PCCP

PAPER

View Article Online
View Journal | View Issue

Cite this: *Phys. Chem. Chem. Phys.*, 2024, **26**, 3880

Te-doped-WSe_2/W as a stable monolith catalyst for ampere-level current density hydrogen evolution reaction†

Xingchen Zhang,[a] Dongfang Zhang,[a] Xinya Chen,[a] Dingyi Zhou,[a] Jinying Zhang [b] and Zhiyong Wang *[a]

The development of efficient electrocatalysts for the hydrogen evolution reaction (HER) holds immense importance in the context of large-scale hydrogen production from water. Nevertheless, the practical application of such catalysts still relies on precious platinum-based materials. There is a pressing need to design high-performing, non-precious metal electrocatalysts capable of generating hydrogen at substantial current levels. We report here a stable monolith catalyst of Te-doped-WSe_2 directly supported by a highly conductive W mesh. This catalyst demonstrates outstanding electrocatalytic performance and stability in acidic electrolytes, especially under high current conditions, surpassing the capabilities of commercial 5% Pt/C catalysts. Specifically, at current densities of 10 and 1200 mA cm^{-2}, it exhibits a minimal overpotential of 79 and 232 mV, along with a small Tafel slope of 55 mV dec^{-1}, respectively. The remarkable catalytic activity of Te–WSe_2 can be attributed to the exceptional electron transfer facilitated by the stable monolithic structure, as well as the abundant and efficient active sites in the material. In addition, density functional theory calculations further indicate that Te doping adjusts H atom adsorption on various positions of WSe_2, making it closer to thermal neutrality compared to the original material. This study presents an innovative approach to develop cost-effective HER electrocatalysts that perform optimally under high current density conditions.

Received 28th November 2023,
Accepted 26th December 2023

DOI: 10.1039/d3cp05790a

rsc.li/pccp

1 Introduction

The remarkable energy density and lack of pollutant emissions make hydrogen an increasingly interesting candidate for renewable and eco-friendly energy.[1–8] One promising method for producing hydrogen on a large scale is the combination of renewable energy sources and water splitting.[9–13] This has led to the development of high-performing and long-lasting electrocatalysts designed specifically for HER. Presently, catalysts based on Pt and Pt-based materials exhibit the highest activity for the HER, but their limited availability and high cost have hindered widespread adoption of water electrolysis technology.[14–19] Considerable efforts are currently being devoted to expediting the development of economically viable and easily accessible catalysts for the hydrogen evolution reaction. This includes the exploration of transition-metal carbides,[20–22] nitrides,[23,24] sulfides,[25–27] oxides[28] and phosphides.[29–31] Within the category of catalysts that are free of platinum-group metals, transition-metal disulfides (TMDs), such as WS_2,[32] WSe_2[33] and WTe_2,[34] have received significant attention and are regarded as promising electrocatalysts for water splitting. Both theoretical predictions and experimental findings suggest that the HER activity of TMDs primarily stems from their edges rather than their basal planes.[35,36]

Various techniques have been devised to improve the catalytic performance of TMDs, such as defect engineering,[37] heterostructure fabrication,[38] phase conversion[39] and foreign atom doping.[40] Wang *et al.* synthesized metallic WSe_2 nanoscrolls used as electrocatalysts for the HER, demonstrating much enhanced electrocatalytic performance compared to the semiconducting 2H WSe_2 nanoscroll counterparts.[41] Zhao *et al.* synthesized NiMo-doped WSe_2 catalyst through a one-step hydrothermal reaction, with overpotentials of 177 and 188 mV at a current density of 10 mA cm^{-2} in 0.5 M H_2SO_4 and 1 M KOH, respectively. Theoretical calculations confirmed that NiMo co-doping significantly reduced the potential energy barrier of HER reaction, and thus improved HER performance.[42] These studies shed light on the considerable potential of WSe_2 as a proficient catalyst for the process of HER, thus revealing its promising prospects in the

---

[a] *Key Laboratory of Advanced Light Conversion Materials and Biophotonics, Department of Chemistry, Renmin University of China, Beijing 100872, PR China. E-mail: zhiyongwang@ruc.edu.cn*

[b] *State Key Laboratory of Electrical Insulation and Power Equipment, Center of Nanomaterials for Renewable Energy (CNRE), School of Electrical Engineering, Xian Jiaotong University, Xian, Shanxi, 710049, PR China*

† Electronic supplementary information (ESI) available. See DOI: **https://doi.org/10.1039/d3cp05790a**

development of hydrogen production techniques. However, the catalytic efficiency of WSe_2 in previous studies does not meet the practical requirements, especially in terms of the high current density needed for industrial production. The objective of this research is to develop an effective approach to enhance the performance of WSe_2 beyond that of Pt/C, in order to enable the industrial implementation of non-precious metal catalysts. In order to achieve this, we utilized a Te doping technique to introduce a significant number of electroactive sites into WSe_2. The WSe_2 material was obtained by selenization of the oxide layer of W meshes. The selenized W mesh can be used as an electrode for HER. Additionally, the W wires play a crucial role in facilitating electron transport. The Te-doped WSe_2 prepared in this manner demonstrates outstanding catalytic properties in acidic environments. Notably, its performance at high current densities exceeds that of the commercially available 5% Pt/C catalyst. We conducted first-principles calculations to gain insight into the reasons behind the improved activity.

2 Experimental

2.1 Sample preparation

The synthesis of the Te-doped WSe_2 catalyst involved a two-zone chemical vapor deposition (CVD) method, as shown in Fig. 1a. A W mesh (1×1 cm^2, 200 mesh) was used as the growth supports. First, the W mesh was cleaned ultrasonically with distilled water and ethanol for 1000 s each. Then, in the CVD furnace, 0.1 g of Se and 0.1 g of Te were placed separately in two porcelain boats in the middle of the T1 zone. The W mesh was positioned in the middle of the T2 zone.

The T1 and T2 zones underwent a gradual heating process, with T1 reaching a temperature of 500 °C and T2 reaching a temperature of 600 °C over a period of 25 min. These temperatures were then maintained for an additional 25 min. Afterwards, both temperature zones were further heated for 15 min until reaching a temperature of 700 °C simultaneously, and this temperature was maintained for 10 min. Throughout the synthesis process, a stream of Ar gas at a flow rate of 100 sccm was continuously passed under ambient pressure until T1 reached a temperature of 400 °C, as shown in Fig. 1b. Following this, a mixture of carrier gases consisting of 100 sccm Ar/H_2 (with a ratio of 9 : 1) was used until the furnace cooled down to room temperature. In order to examine the effect of Te doping on the enhancement of catalytic performance of WSe_2, both WSe_2 and WTe_2 were synthesized under identical conditions for comparative analysis.

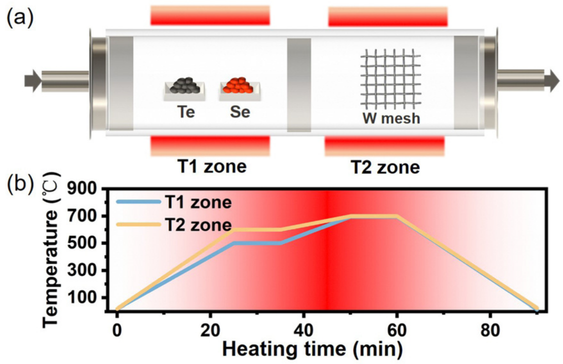

Fig. 1 (a) Schematic illustration of the high-temperature reaction system used for the synthesis of Te–WSe_2. (b) Temperature–time profiles for the synthesis of Te–WSe_2.

Preparation of Pt/C electrodes involves the following steps: 490 μL of water, 490 μL of ethanol, 20 μL of 5% Nafion solution and 3 mg of Pt/C were mixed together and subjected to ultrasound for 1 hour. Then, 10 μL of the mixture were applied as drops onto a circular glassy carbon electrode with a 5 mm diameter for electrochemical testing.

2.2 Characterization

Scanning electron microscopy (SEM) images were obtained using a Hitachi SU-8010 instrument. High-resolution transmission electron microscopy (HRTEM) images were recorded using an FEI Tecnai G2 F30 microscope under an acceleration voltage of 300 kV. Raman spectra were recorded on a Horiba Xplora spectrophotometer with a 532 nm laser. Structural and chemical analyses of the samples were performed using powder X-ray diffractometer (XRD 7000 X-ray) with Cu Kα radiation (λ = 1.54 Å) and X-ray photoelectron spectroscopy (XPS, Thermo Scientific K-Alpha).

2.3 Electrochemical measurements

The electrochemical measurements were performed on an electrochemical workstation (CHI660E). The W mesh supporting Te–WSe_2 catalysts was used as the working electrode, and Ag/AgCl and Pt electrodes were used as the reference and counter electrodes, respectively. All the potentials mentioned are in reference to the reversible hydrogen electrode (RHE): $E_{\mathrm{RHE}} = E_{(\mathrm{Ag/AgCl})} + 0.059 \times \mathrm{pH} + 0.197$ V. The electrochemical measurements were carried out in 0.5 M H_2SO_4. High-purity Ar gas was bubbled into the electrolyte for 30 min before the measurements. Linear sweep voltammetry (LSV) measurements were conducted between 0 and −0.6 V *versus* Ag/AgCl at a scan rate of 5 mV s^{-1}. All results were corrected by 95% ohmic potential drop (iR) correction. The Tafel curve was obtained from the LSV curves. Electrochemical impedance spectroscopy (EIS) was conducted at an overpotential of 50 mV and in the frequency range of 1000–10 Hz with an amplitude of 5 mV, and then Z-view software was used to select a suitable equivalent circuit for fitting. The value of the double-layer capacitance (C_{dl}) was calculated by testing typical CV curves in 0 to 0.2 V *versus* RHE at different scan rates (20, 40, 60, 80, 100, 120, 140, 160, 180, and 200 mV s^{-1}). The electrochemical double layer capacitance (C_{dl}) values is the slope of plotting $\Delta J/2(\Delta J = j_{\mathrm{anodic}} - j_{\mathrm{cathodic}})$ at 0.1 V against scan rates. Long-term stability tests were performed using 16 h chronopotentiometry (CP) test under different current densities.

2.4 Computational details

First-principles calculations in the framework DFT are performed by using the Vienna ab initio simulation package (VASP)[43–45] with the projector–augmented wave method (PAW). The exchange–correlation energy was calculated by using the generalized gradient approximation (GGA) of Perdew–Burke–Ernzerhof (PBE).[46] The energy cutoff is set to 400 eV. Spin polarization effects are considered in this study. We performed structural optimization until the residual forces on each ion converged to less than 0.01 eV. The adsorption energy for surface hydrogen adsorbates is defined as follows: $\Delta E_H = E_{adsorption} - E_{surface} - 0.5 \times E_{H_2(g)}$, where $E_{adsorption}$ represents the energy of the surface with the adsorbed hydrogen atom, $E_{surface}$ represents the energy of the pure surface, and $E_{H_2(g)}$ represents the energy of the H_2 species in the gas phase. The calculation also includes entropy (S) and zero-point energy (ZPE) to obtain the Gibbs free adsorption energy of hydrogen: $\Delta G_H = \Delta E_H + \Delta E_{ZPE} - T\Delta S$.

3 Results and discussion

The surface morphology of the W mesh was analyzed using scanning electron microscopy (SEM) both before and after the CVD reaction. Initially, the W mesh displayed a fairly even surface with slight surface striations (Fig. 2a). Following the reaction, a significant transformation occurred, resulting in a textured "accordion-like" surface with distinct split stripes (as shown in Fig. 2b). In order to conduct a more detailed examination, the W wire was carefully dissected to reveal its cross section (Fig. 2c). This revealed the growth of layered structures on the surface of the W wire, which corresponded to the Te doped WSe_2 layers.

HRTEM was utilized to investigate the microstructure and elemental composition of the products. The HRTEM image of Te–WSe_2, depicted in Fig. 3a, reveals a layered structure with small grain coverage. Fig. 3b showcases the edge of Te–WSe_2, where a crystal lattice spacing of 0.28 nm corresponds to the (100) plane of WSe_2. The sample exhibits abundant structural defects, such as irregular edges and internal micro pores, which can potentially act as active sites for catalysis. Fig. 3c displays the selected-area electron diffraction (SAED) pattern of the products, clearly identifying the crystal planes including (011), (013), (008), (023), and (−130) of WSe_2. Additionally, the STEM-HAADF images, along with EDS elemental mapping of W, Se, and Te elements (as shown in Fig. 3d), validate the uniform distribution of Te within WSe_2, thereby confirming the successful synthesis of Te–WSe_2.

The chemical composition and electronic states of the Te–WSe_2 sample were analyzed by using XPS measurements. The XPS spectra reveal the presence of Te, Se, and W elements, confirming their coexistence in the sample. As shown in Fig. 4a, two characteristic peaks observed at 573.20 eV and 583.71 eV corresponded to Te $3d_{5/2}$ and Te $3d_{3/2}$ states, respectively. The XPS spectrum of Te $3d_{5/2}$ and Te $3d_{3/2}$ at 573.20 eV and 583.71 eV corresponding to the Te^{2-} state, indicating the successful doping of Te with a doping concentration of 0.65%. The W 4f elemental binding energy profile in Fig. 4b displayed two prominent peaks at 32.63 eV and 34.63 eV, corresponding to W $4f_{7/2}$ and W $4f_{5/2}$ states in Te–WSe_2, respectively. Additionally, the peaks observed at 54.51 eV and 55.33 eV were attributed to Se $3d_{5/2}$ and Se $3d_{3/2}$ states in Te–WSe_2 (as shown in Fig. 4c). As compared to WSe_2 (XPS spectra are shown in Fig. S1, ESI†), the Se $3d_{3/2}$ and Se $3d_{5/2}$ peaks in Te–WSe_2 exhibited a shift of −0.4 eV and −0.37 eV, respectively. This shift in Se 3d peaks can be attributed to the reduced electron attraction strength of Te and the enhanced electron attraction strength of Se. Consequently, the electron density surrounding Se increased due to the introduction of Te, which possesses a relatively lower electronegativity compared to Se.

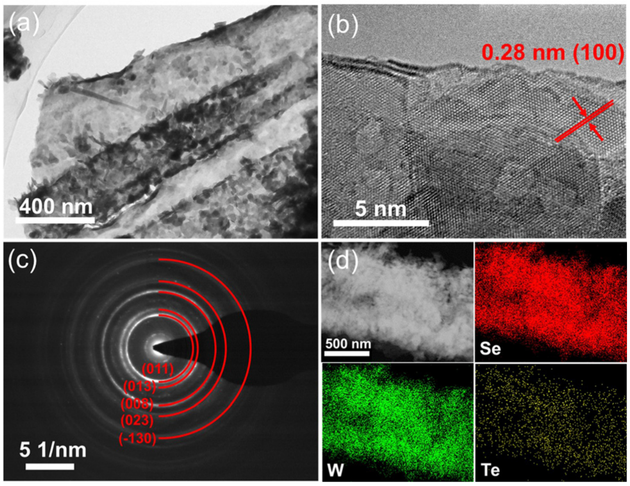

Fig. 3 (a) and (b) HRTEM images of Te–WSe_2. (c) SAED pattern of Te–WSe_2. (d) STEM-HAADF with EDS elemental mapping images of Se, W, Te.

Raman spectrum of Te–WSe_2 under 532 nm laser excitation reveals the characteristic in-plane E^1_{2g} peak of WSe_2 at 250 cm^{-1} (Fig. 5a). With the introduction of Te, the peak shifts to a lower frequency (246.9 cm^{-1}) and the intensity decreases. This frequency shift suggests that Te doping causes soft W–Se vibrations. Additionally, the reduced Raman intensity is likely a

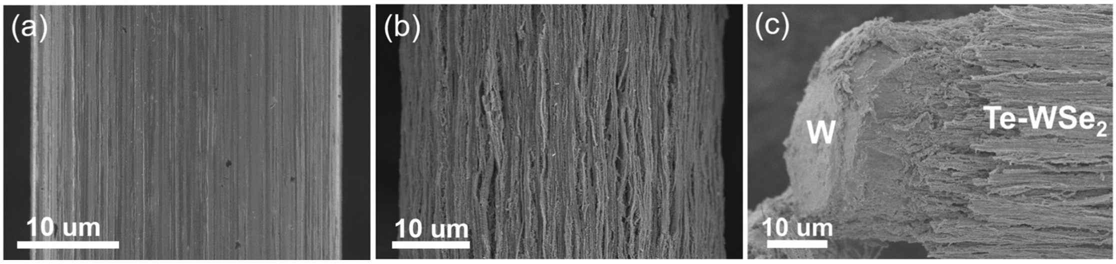

Fig. 2 (a) SEM image of the original W mesh. (b) and (c) SEM images of Te–WSe_2/W.

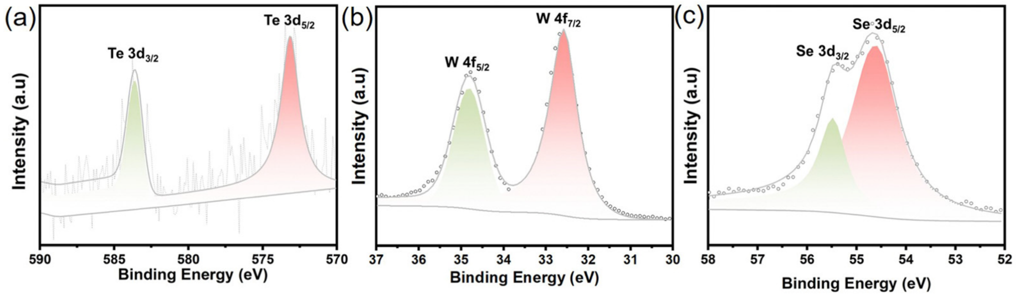

Fig. 4 XPS spectra of Te–WSe_2 showing the signals of (a) Te 3d, (b) W 4f and (c) Se 3d.

result of the change in lattice symmetry, which affects the matrix elements and selection rules for Raman active vibrational modes. XRD spectra were measured to confirm the composition of the products. Fig. 5b illustrates the XRD patterns of Te–WSe_2 and WSe_2, with the observed peaks for WSe_2 aligning well with the standard 2H-WSe_2 PDF card (JCPDS no. 38-1388). The XRD spectrum peaks show no significant change upon Te doping, indicating that the original structure of 2H-WSe_2 remains unchanged.

To evaluate the electrochemical catalytic potential of Te–WSe_2, we conducted a three-electrode cell experiment using an Ar-saturated 0.5 M H_2SO_4 electrolyte. Additionally, we measured the HER performance of the prepared WSe_2 and WTe_2 samples to understand the impact of Te doping. The catalytic properties of the samples were evaluated through LSV analysis, and the polarization curves of the different catalysts can be seen in Fig. 6a. By comparing the overpotentials at current densities of 10, 100, 500, and 1200 mA cm^{-2}, we were able to determine the catalyst activities (Fig. 6b). The results indicated a significant improvement in the catalytic performance of WSe_2 after Te doping. For the original WSe_2, the overpotentials at current density of 10, 100, 500, and 1200 mA cm^{-2} were measured as 366, 461, 525, and 541 mV, respectively. However, after Te doping, the overpotentials decreased significantly to 79, 170, 207, and 232 mV, respectively. Moreover, as the current density increased, the advantage of Te–WSe_2 became increasingly prominent. In fact, the sample achieved a high current density of 1000 mA cm^{-2} with a low overpotential of 225 mV, surpassing both the commercial 5% Pt/C catalyst and most reported high current density catalysts (Table 1). We have prepared a series of Te-doped WSe_2 samples by varying the quantity of Te reactant. It was observed that the sample produced with 0.1 g of Te demonstrated the most favorable catalytic performance (Fig. S2, ESI†).

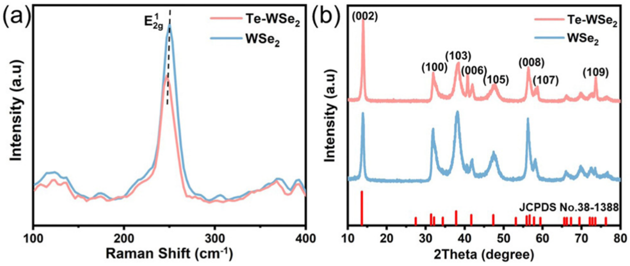

Fig. 5 (a) and (b) Raman scattering spectra and XRD pattern of Te–WSe_2 and WSe_2. The curves denoted with pink and blue colors correspond to signals from Te–WSe_2 and WSe_2.

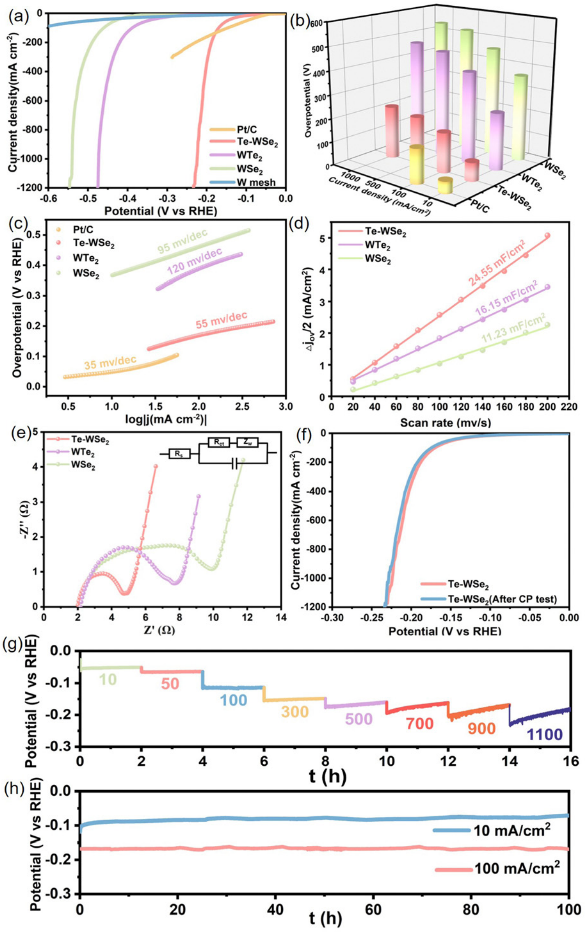

Fig. 6 (a) The polarization curves, (b) overpotentials at different current densities and (c) the calculated Tafel slopes for Te–WSe_2, WSe_2, WTe_2 and 5% Pt/C catalyst. The measurements were performed in 0.5 M H_2SO_4 at a scan rate of 5 mV s^{-1}. (d) The double-layer capacitance (C_{dl}) and (e) Nyquist plots for Te–WSe_2, WSe_2, WTe_2. (f) The polarization curves for Te–WSe_2 before and after 16 h CP test. (g) 16 h CP test at different current densities (mA cm^{-2}). (h) 100 h CP test at current densities of 10 and 100 mA cm^{-2}.

Table 1 The electrochemical catalytic performance of high current-density catalysts

Electrocatalyst	Electrolyte	Current density (mA cm^{-2})	Overpotential (mV)	Tafel slope (mV dev^{-1})
Te–WSe$_2$ (this work)	0.5 M H_2SO_4	10	79	55
		100	170	
		500	207	
		1000	225	
CuMo$_6$S$_8$/Cu[47]	1 M KOH	10	172	43
		1000	320	
P/Mo–Ni$_3$S$_2$/NF[48]	0.5 M H_2SO_4	1000	240	75
α-MoB$_2$[49]	0.5 M H_2SO_4	10	149	74.2
		1000	334	
WS$_{2(1-x)}$Se$_{2x}$/NiSe$_2$[50]	0.5 M H_2SO_4	10	88	74.2
		400	≈175	
CH$_4$/H$_2$ thermal treatment[51] MoS$_2$/Mo$_2$C	0.5 M H_2SO_4	1000	412	60
α-MoWS$_x$/N-RGO[52]	0.5 M H_2SO_4	1000	349	43
CoP/Ni$_5$P$_4$/CoP[53]	0.5 M H_2SO_4	10	33	43
		500	≈130	
		1000	142	
NiP$_2$/Ni$_5$P$_4$/CoPS/CoP$_3$[54]	0.5 M H_2SO_4	10	41	45.2
		100	88	
		500	130	
		1000	150	
Ni$_5$P$_4$@Cu foam[55]	0.5 M H_2SO_4	10	90	49
		100	164	
		1000	≈230	
MoS$_2$/Mo$_2$C[56]	0.5 M H_2SO_4	1000	227	53
MoS$_x$–Fe@UiO-66-(OH)$_2$[57]	0.5 M H_2SO_4	10	118	41
		1000	297	
Co/Se–MoS$_2$-NF[36]	0.5 M H_2SO_4	10	104	67
		100	188	
		1000	382	
Rh/SiNW[58]	0.5 M H_2SO_4	10	180	24
		1000	950	
2H Nb$_{1.35}$S$_2$[59]	0.5 M H_2SO_4	1000	370	43
Co–Co$_2$P@N,P doped C/rGO[60]	0.5 M H_2SO_4	10	130	50.64
		1000	900	
MoS$_2$/CNF[61]	0.5 M H_2SO_4	500	380	69
		1000	450	
MoS$_2$/graphene[13]	0.5 M H_2SO_4	10	62	43.3
		1000	250	
Ni$_2$P–CuP$_2$[62]	0.5 M H_2SO_4	10	12	41
		100	124	
		1000	≈500	
Co–N doped C[63]	0.5 M H_2SO_4	500	272	67.6
		1000	343	
α-MoS$_x$[64]	0.5 M H_2SO_4	10	68	86
		100	80	
		500	250	
		1000	322	
MoSe$_2$/MoO$_2$[65]	0.5 M H_2SO_4	10	140	48.9
		200	≈350	

The relative activity of the catalysts was further compared by the Tafel slope (Fig. 6c). The Tafel slope is an inherent characteristic of electrocatalysts and is indicative of the rate-limiting step in HER. We fitted the experimental data from the polarization curve to the Tafel equation and calculated the Tafel slope ($\eta = b\log j + a$) from the linear portion of the Tafel plot, where "b" represents the Tafel slope. In acidic electrolytes, the typical mechanism of electrochemical hydrogen evolution involves three main steps: Volmer, Heyrovsky, and Tafel reactions, each associated with Tafel slopes of approximately 120, 40, and 30 mV dec^{-1}, respectively.[66] Pt/C has the best catalytic performance, with a Tafel slope of 35 mV dec^{-1}. The prepared

Table 2 HER catalytic activity parameters obtained from electrochemical tests

Cathodes	η_{10} (mV)	η_{1200} (mV)	Tafel slope (mV dec^{-1})	R_s (Ω cm^2)	R_{ct} (Ω cm^2)	ECSA (cm^2)
Pt/C	50	—	35	—	—	—
Te–WSe$_2$	79	232	55	2.008	2.68	701.4
WSe$_2$	366	541	95	2.107	9.08	320.9
WTe$_2$	243	476	120	2.155	5.88	461.4

WSe_2 and WTe_2 exhibit Tafel slopes of 95 mV dec^{-1} and 120 mV dec^{-1}, respectively, indicating that both have high initial energy barriers and slow reaction rates in the HER process. After successful incorporation of Te into WSe_2, Te–WSe_2 exhibits a Tafel slope of 55 mV dec^{-1}, indicating that the Heyrovsky–Volmer reaction is its main pathway in the HER reaction process. The comparison of Te–WSe_2 with WSe_2 and WTe_2 indicates that the introduction of Te effectively accelerates the kinetic process of the catalytic reaction, thereby improving the activity of the catalyst.

To elucidate the reason behind the superior hydrogen evolution performance of Te–WSe_2, we analyzed the electrochemical active surface areas (ECSA) of the catalysts. The ECSA was evaluated by double-layer capacitance (C_{dl}) using cyclic voltammetry at various scan rates in the potential range from 0 to 0.2 V *versus* RHE (Fig. S4 in ESI†). Typically, the ECSA is directly proportional to the C_{dl} of the electrode, expressed as ECSA = C_{dl}/C_s, where C_s represents the specific capacitance of the catalysts per unit area under identical electrolyte conditions. The specific capacitance typically falls within a reported range of 0.015–0.110 mF cm^{-2} in acidic solutions. The general specific capacitance of 0.035 mF cm^{-2} was used to estimate ECSA in this work.[67] The C_{dl} of WSe_2 increased after Te doping (Fig. 6d), indicating a positive effect of Te doping on the electrochemical activity. Te–WSe_2 electrode has the largest ECSA of 701.4 cm^2, indicating the presence of a greater number of active sites. The order of ECSA among the different samples aligns with the catalytic performance observed in the LSV plots, indicating that the active surface area is an important factor that determines the catalytic properties. It should be noted that the active surface area of the Te–WSe_2 electrode is much larger than WSe_2 (320.9 cm^2) and WTe_2 (461.4 cm^2), implying that Te doping leads to the formation of more active sites. The calculated ECSA values are summarized in Table 2.

EIS serves as a valuable technique for investigating the kinetics of electron transfer in the HER. The solution resistance (R_s) signifies the overall resistance within the electrolyte, while the diameter of the semicircle in the high-frequency range reflects the charge transfer resistance (R_{ct}). As depicted in Fig. 6e, all catalysts demonstrate comparable R_s values, implying similar solution resistance. However, when comparing the charge transfer resistance, Te–WSe_2 exhibited the lowest R_{ct} at 2.68 Ω cm^2, while WSe_2 and WTe_2 displayed higher resistances of 9.08 Ω cm^2 and 5.88 Ω cm^2, respectively. The reduction in resistance following Te doping signifies favorable reaction kinetics and effective charge transfer within Te–WSe_2.

The stability of a catalyst is a key parameter for evaluating its performance.[68,69] In Fig. 6g, a 16 h CP test is illustrated, demonstrating that Te–WSe_2 maintains stability across varying current densities: 10, 50, 100, 300, 500, 700, 900, and 1100 mA cm^{-2}. It can be seen that Te–WSe_2 exhibits stable operation under diverse current densities without notable overpotential escalation. Notably, at large current densities of 900 and 1100 mA cm^{-2}, the overpotential significantly diminishes with prolonged operation, signifying the successful activation and robust stability of Te–WSe_2. Fig. 6h illustrates the 100 h CP tests at current densities of 10 and 100 mA cm^{-2}, further proving the stability of the catalyst. Fig. 4f shows the polarization curves before and after CP test. It can be seen that the electrode exhibits a high stability toward the HER with very small cathodic current loss. After CP testing, Raman and SEM measurements confirmed the retention of the original structure of the catalyst (Fig. S5 and S6, ESI†).

In comparison to previously reported MoX_2 (X = S, Se, or Te) catalysts, the Te–WSe_2 catalyst featured in this study showcases superior catalytic performance, particularly at elevated current densities. The catalytic performance of Te–WSe_2 is related to the electrode's microstructure. Te–WSe_2 is cultivated on a metallic W mesh substrate, resulting in a stable monolithic catalyst (Fig. 2c and 7a). The Te–WSe_2 layers are directly supported by the highly conductive metal mesh, ensuring a strong supply of electrons to each layer of Te–WSe_2. As such, electron transport within the Te–WSe_2 layers is facilitated. This arrangement exhibits exceptional overall conductivity, leading to outstanding catalytic performance even at high current densities. Furthermore, the distinct stripes within the ''accordion-like'' texture reveal a substantial active surface area within the material. Additionally, the specimen exhibits numerous structural defects, including irregular edges and internal microporous structures, all of which can function as highly effective catalytic active sites.

We subsequently explore the potential of Te–WSe_2 as a catalyst for the hydrogen evolution reaction in practical settings. The catalytic performance of bipolar catalysts at the cathode and

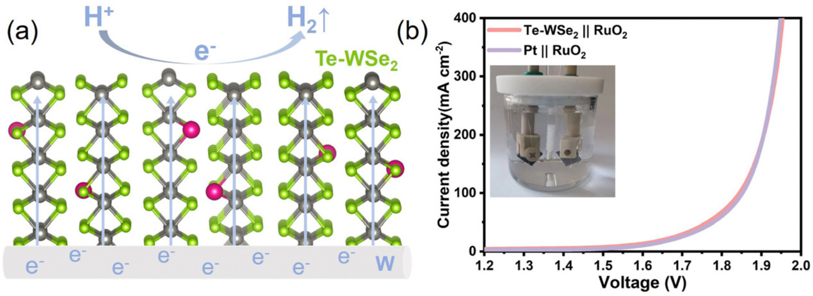

Fig. 7 (a) Schematic diagram showing electron transport in Te–WSe_2/W. (b) Polarization curves of two-electrode overall water splitting performed in 0.5 M H_2SO_4 at a scanning rate of 5 mV s^{-1}. RuO_2 serves as the anode, while Te–WSe_2 and Pt/C are employed as cathodes, respectively. Inset: A photograph of the overall water splitting system.

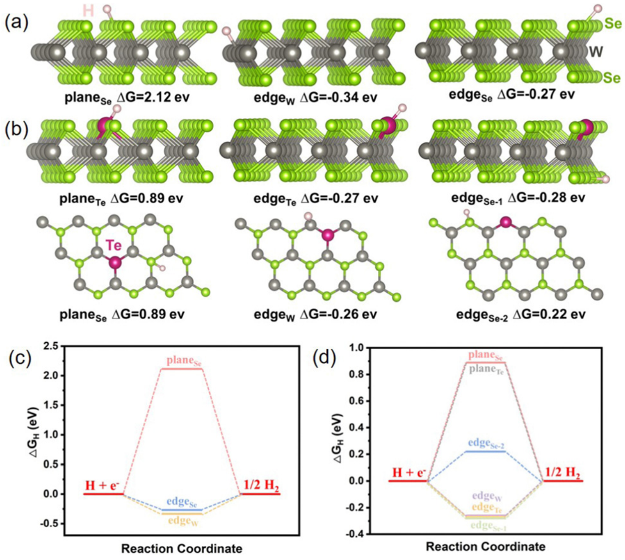

Fig. 8 (a) and (b) DFT-optimized structures showing H atom adsorption on different positions of WSe_2 and Te–WSe_2. (c) and (d) The calculated ΔG for H atom adsorption on different positions of Te–WSe_2 and WSe_2.

anode plays a pivotal role in the overall efficiency of water hydrolysis. To evaluate this, we employed commercial RuO_2 as the anode catalyst and conducted a comparative analysis of Te–WSe_2 and commercial Pt/C as cathode catalysts in the water hydrolysis experiment. This experiment was carried out in an acidic solution with a concentration of 0.5 M H_2SO_4. Significantly, the catalysts Te–WSe_2‖RuO_2 and Te–WSe_2‖Pt/C exhibited remarkably similar performance, as evidenced by their comparable overpotentials at different current densities (as shown in Fig. 7b). This finding highlights the potential of Te–WSe_2 as a highly effective catalyst for hydrogen evolution, thus indicating its promising prospects for industrial applications.

To gain deeper insights into the active sites of Te–WSe_2 in the context of catalyzing the HER, we conducted DFT calculations on both Te–WSe_2 and WSe_2. The catalyst's activity can be assessed by the calculated Gibbs free energy (ΔG), which is associated with the adsorption of hydrogen atoms onto the material's surface.[70] Effective HER catalysts usually exhibit ΔG values close to zero,[71] indicating a balanced hydrogen adsorption strength. If ΔG is excessively positive, hydrogen adsorption becomes challenging, impeding the reaction. Conversely, an excessively negative ΔG results in strong hydrogen adsorption, leading to catalyst poisoning. Thus, an ideal HER catalyst should exhibit a ΔG value close to 0 eV. In our study, we investigated H adsorption at various positions on Te–WSe_2, including basal plane ($plane_{Se}$), doped Te atom at the basal plane ($plane_{Te}$), metal edge ($edge_W$), and non-metallic edge ($edge_{Te}$, $edge_{Se}$). For comparison, we also computed H atom adsorption at the basal plane ($plane_{Se}$), metal edge ($edge_W$), and non-metallic edge ($edge_{Se}$) of WSe_2. The optimized structures and calculated ΔG values are shown in Fig. 8a–c. The pristine WSe_2 exhibits ΔG values of 2.12, −0.34, and −0.27 eV for hydrogen atom adsorption at the basal plane, W edge, and Se edge, respectively. In the case of Te–WSe_2, the ΔG value for hydrogen atom adsorption at the Se site of the basal plane ($plane_{Se}$) decreases to 0.89 eV, while the ΔG value for Te site of the basal plane ($plane_{Te}$) is also calculated to be 0.89 eV. The ΔG value for hydrogen atom adsorption at the metal edge ($edge_W$) is −0.26 eV, which is closer to zero compared to pristine WSe_2. The ΔG value for hydrogen atom adsorption at the Te site of the edge ($edge_{Te}$) is −0.27 eV. The calculated ΔG values for edge Se sites in proximity to the Te atom ($edge_{Se1}$ and $edge_{Se2}$) are −0.28 eV and 0.22 eV, respectively. Based on these findings, Te doping of WSe_2 has the potential to promote the adsorption of hydrogen atoms in a reversible manner, thus improving the electrocatalytic properties.

4 Conclusions

In this research, we synthesized WSe_2 doped with Te and investigated its electrocatalytic capabilities for HER. To enhance the performance of Te–WSe_2, we directly deposited it onto a highly conductive W mesh, resulting in a stable monolith catalyst that greatly enhances electron transport and conductivity. The material exhibits numerous irregular edges and an internal microporous structure, thereby exposing a significant number of active sites. Moreover, our computational analysis demonstrates that Te doping effectively reduces ΔG of the active sites and enhances the catalytic activity of the sites. Consequently, the material exhibits outstanding catalytic performance even at high current densities. Specifically, at current densities of 10 100, 500, and 1000 mA cm^{-2}, the overpotentials are 79, 170, 207 and 225 mV, respectively, with a Tafel slope of 55.0 mV dec^{-1}. This study introduces a novel approach for developing cost-effective HER electrocatalysts that function effectively under high current density conditions.

Conflicts of interest

There are no conflicts to declare.

Acknowledgements

This work was supported by Public Computing Cloud, Renmin University of China.

Notes and references

1 Z. Shi, X. Zhang, X. Lin, G. Liu, C. Ling, S. Xi, B. Chen, Y. Ge, C. Tan and Z. Lai, *et al.*, Phase-dependent growth of Pt on MoS_2 for highly efficient H_2 evolution, *Nature*, 2023, **621**, 300–305.
2 C. Zhang, Z. Xu, N. Han, Y. Tian, T. Kallio, C. Yu and L. Jiang, Superaerophilic/superaerophobic cooperative electrode for efficient hydrogen evolution reaction via enhanced mass transfer, *Sci. Adv.*, 2023, **9**, eadd6978.
3 H. Yu, S. Zhu, Y. Hao, Y.-M. Chang, L. Li, J. Ma, H.-Y. Chen, M. Shao and S. Peng, Modulating Local Interfacial Bonding Environment of Heterostructures for Energy-Saving

Hydrogen Production at High Current Densities, *Adv. Funct. Mater.*, 2023, **33**, 2212811.

4 D. Qiao, S. Yun, M. Sun, J. Dang, Y. Zhang, S. Yuan, G. Yang, T. Yang, Z. Gao and Z. Wang, 1D/3D trepang-like N-modified carbon confined bimetal carbides and metal cobalt: boosting electron transfer via dual Mott–Schottky heterojunctions triggered built-in electric fields for efficient hydrogen evolution and tri-iodide reduction, *Appl. Catal., B*, 2023, **334**, 122830.

5 L. Wang, Y. Hao, L. Deng, F. Hu, S. Zhao, L. Li and S. Peng, Rapid complete reconfiguration induced actual active species for industrial hydrogen evolution reaction, *Nat. Commun.*, 2022, **13**, 5785.

6 S. Sarwar, A. Ali, Y. Wang, M. R. Ahasan, R. Wang, A. J. Adamczyk and X. Zhang, Enhancement of hydrogen evolution reaction activity using metal–rich molybdenum sulfotelluride with graphene support: a combined experimental and computational study, *Nano Energy*, 2021, **90**, 106599.

7 Z.-Y. Zhang, H. Tian, L. Bian, S.-Z. Liu, Y. Liu and Z.-L. Wang, Cu–Zn-based alloy/oxide interfaces for enhanced electroreduction of CO_2 to C^{2+} products, *J. Energy Chem.*, 2023, **83**, 90–97.

8 L. Bian, Z.-Y. Zhang, H. Tian, N.-N. Tian, Z. Ma and Z.-L. Wang, Grain boundary-abundant copper nanoribbons on balanced gas-liquid diffusion electrodes for efficient CO_2 electroreduction to C_2H_4, *Chin. J. Catal.*, 2023, **54**, 199–211.

9 Q. Fu, L. W. Wong, F. Zheng, X. Zheng, C. S. Tsang, K. H. Lai, W. Shen, T. H. Ly, Q. Deng and J. Zhao, Unraveling and leveraging in situ surface amorphization for enhanced hydrogen evolution reaction in alkaline media, *Nat. Commun.*, 2023, **14**, 6462.

10 C. D. Abernethy, G. M. Codd, M. D. Spicer and M. K. Taylor, A highly stable N-heterocyclic carbene complex of trichloro-oxovanadium(v) displaying novel Cl–C(carbene) bonding interactions, *J. Am. Chem. Soc.*, 2003, **125**, 1128–1129.

11 S. Zhao, L. Yin, L. Deng, J. Song, Y.-M. Chang, F. Hu, H. Wang, H.-Y. Chen, L. Li and S. Peng, Inheritable Organic-Inorganic Hybrid Interfaces with π–d Electron Coupling for Robust Electrocatalytic Hydrogen Evolution at High-Current-Densities, *Adv. Funct. Mater.*, 2023, **33**, 2211576.

12 J. Dang, S. Yun, Y. Zhang, G. Yang, J. Yang, D. Qiao and T. Yang, Designing nitrogen-enriched heterogeneous NiS@$CoNi_2S_4$ embedded in nitrogen-doped carbon with hierarchical 2D/3D nanocage structure for efficient alkaline hydrogen evolution and triiodide reduction, *J. Colloid Interface Sci.*, 2023, **630**, 91–105.

13 S. Sarwar, A. Nautiyal, J. Cook, Y. Yuan, J. Li, S. Uprety, R. Shahbazian-Yassar, R. Wang, M. Park and M. J. Bozack, *et al.*, Facile microwave approach towards high performance MoS_2/graphene nanocomposite for hydrogen evolution reaction, *Sci. China: Mater.*, 2020, **63**, 62–74.

14 L. Wang, L. Song, Z. Yang, Y.-M. Chang, F. Hu, L. Li, L. Li, H.-Y. Chen and S. Peng, Electronic Modulation of Metal–Organic Frameworks by Interfacial Bridging for Efficient pH-Universal Hydrogen Evolution, *Adv. Funct. Mater.*, 2023, **33**, 2210322.

15 C. Wan, Z. Zhang, J. Dong, M. Xu, H. Pu, D. Baumann, Z. Lin, S. Wang, J. Huang and A. H. Shah, *et al.*, Amorphous nickel hydroxide shell tailors local chemical environment on platinum surface for alkaline hydrogen evolution reaction, *Nat. Mater.*, 2023, 1–8.

16 Z. Ren, H. Jiang, M. Yuan, Z. Xie, L. Deng, J. Han, K. Lyu, Y. Zhu, X. Li and L. Zhuang, Si regulation of hydrogen adsorption on nanoporous PdSi hybrids towards enhancing electrochemical hydrogen evolution activity, *Inorg. Chem. Front.*, 2023, **10**, 1101–1111.

17 J. Zhang, X. Zhang, C. Shi, G. Xia, H. Li, P. Wang and L. Di, Plasma synthesis of defect-rich flexible carbon cloth decorated with PtRu alloyed nanoclusters for highly efficient pH-universal electrocatalytic hydrogen evolution, *Nanoscale*, 2022, **14**, 15942–15949.

18 Y. Wang, S. Yun, J. Shi, Y. Zhang, J. Dang, C. Dang, Z. Liu, Y. Deng and T. Yang, Defect engineering tuning electron structure of biphasic tungsten-based chalcogenide heterostructure improves its catalytic activity for hydrogen evolution and triiodide reduction, *J. Colloid Interface Sci.*, 2022, **625**, 800–816.

19 M. Luo, J. Yang, X. Li, M. Eguchi, Y. Yamauchi and Z.-L. Wang, Insights into alloy/oxide or hydroxide interfaces in Ni–Mobased electrocatalysts for hydrogen evolution under alkaline conditions, *Chem. Sci.*, 2023, **14**, 3400–3414.

20 C. Yang, R. Zhao, H. Xiang, J. Wu, W. Zhong, W. Li, Q. Zhang, N. Yang and X. Li, Ni-activated transition metal carbides for efficient hydrogen evolution in acidic and alkaline solutions, *Adv. Energy Mater.*, 2020, **10**, 2002260.

21 K. Liang, A. Tabassum, M. Kothakonda, X. Zhang, R. Zhang, B. Kenney, B. D. Koplitz, J. Sun and M. Naguib, Twodimensional titanium carbonitride MXene as a highly efficient electrocatalyst for hydrogen evolution reaction, *Mater. Rep.: Energy*, 2022, **2**, 100075.

22 Y. Li, S. Zhu, E. Wu, H. Ding, J. Lu, X. Mu, L. Chen, Y. Zhang, J. Palisaitis and K. Chen, *et al.*, Nanolaminated ternary transition metal carbide (MAX phase)-derived core–shell structure electrocatalysts for hydrogen evolution and oxygen evolution reactions in alkaline electrolytes, *J. Phys. Chem. Lett.*, 2023, **14**, 481–488.

23 F. Ma, S. Wang, X. Gong, X. Liu, Z. Wang, P. Wang, Y. Liu, H. Cheng, Y. Dai and Z. Zheng, *et al.*, Highly efficient electrocatalytic hydrogen evolution coupled with upcycling of microplastics in seawater enabled via Ni_3N/W_5N_4 janus nanostructures, *Appl. Catal., B*, 2022, **307**, 121198.

24 Z. Qi, Y. Zeng, Z. Hou, W. Zhu, B. Wei, Y. Yang, B. Lin and H. Liang, Heterointerface engineering of Ni/Ni_3N hierarchical nanoarrays for efficient alkaline hydrogen evolution, *Nano Res.*, 2023, **16**, 4803–4811.

25 P. Da, Y. Zheng, Y. Hu, Z. Wu, H. Zhao, Y. Wei, L. Guo, J. Wang, Y. Wei and S. Xi, *et al.*, Synthesis of Bandgaptunable Transition Metal Sulfides through Gas-phase Cation Exchange-induced Topological Transformation, *Angew. Chem.*, 2023, **135**, e202301802.

26 X. Chen, Z. Han, B. Zhang, B. Sun, Y. Wang, Y. Du, X. Han and P. Xu, Construction of plasmonic 1T-WS_2/2H-WS_2/CdS

heterostructures for enhanced solar driven hydrogen evolution, *J. Mater. Chem. A*, 2022, **10**, 24030–24040.

27 S.-F. Chen, T.-S. Wu and Y.-L. Soo, Highly defective graphene quantum dots-doped 1T/2H-MoS_2 as an efficient composite catalyst for the hydrogen evolution reaction, *Sci. Rep.*, 2023, **13**, 15184.

28 J. Yang, Y. Cao, S. Zhang, Q. Shi, S. Chen, S. Zhu, Y. Li and J. Huang, Interstitial Hydrogen Atom to Boost Intrinsic Catalytic Activity of Tungsten Oxide for Hydrogen Evolution Reaction, *Small*, 2023, 2207295.

29 Q. Liu, Z. Xue, B. Jia, Q. Liu, K. Liu, Y. Lin, M. Liu, Y. Li and G. Li, Hierarchical nanorods of MoS_2/MoP heterojunction for efficient electrocatalytic hydrogen evolution reaction, *Small*, 2020, **16**, 2002482.

30 J. Jin, J. Ge, X. Zhao, Y. Wang, F. Zhang and X. Lei, An amorphous NiCuFeP@Cu_3P nanoarray for an efficient hydrogen evolution reaction, *Inorg. Chem. Front.*, 2022, **9**, 1446–1455.

31 M. R. Kandel, U. N. Pan, P. P. Dhakal, R. B. Ghising, T. T. Nguyen, J. Zhao, N. H. Kim and J. H. Lee, Unique heterointerface engineering of Ni_2P–MnP nanosheets coupled Co_2P nanoflowers as hierarchical dual-functional electrocatalyst for highly proficient overall water-splitting, *Appl. Catal., B*, 2023, **331**, 122680.

32 L. Sun, M. Gao, Z. Jing, Z. Cheng, D. Zheng, H. Xu, Q. Zhou and J. Lin, 1T-Phase Enriched P doped WS_2 nanosphere for highly efficient electrochemical hydrogen evolution reaction, *Chem. Eng. J.*, 2022, **429**, 132187.

33 C.-H. Chiang, Y.-C. Yang, J.-W. Lin, Y.-C. Lin, P.-T. Chen, C.-L. Dong, H.-M. Lin, K. M. Chan, Y.-T. Kao and K. Suenaga, *et al.*, Bifunctional monolayer WSe_2/graphene self-stitching heterojunction microreactors for efficient overall water splitting in neutral medium, *ACS Nano*, 2022, **16**, 18274–18283.

34 D. Xia, Z. Wang, S. Yang, Z. Cai, M. Hu, H. He and K. Zhou, Enhancing electrocatalytic hydrogen evolution of WTe_2 by formation of amorphous phosphate nanoshells, *Electrochim. Acta*, 2021, **385**, 138409.

35 Y. Tan, J. Feng, H. Dong, L. Liu, S. Zhao, F. Lai, T. Liu, Y. Bai, I. P. Parkin and G. He, The edge effects boosting hydrogen evolution performance of platinum/transition bimetallic phosphide hybrid electrocatalysts, *Adv. Funct. Mater.*, 2023, **33**, 2209967.

36 Z. Zheng, L. Yu, M. Gao, X. Chen, W. Zhou, C. Ma, L. Wu, J. Zhu, X. Meng and J. Hu, *et al.*, Boosting hydrogen evolution on MoS_2 via co-confining selenium in surface and cobalt in inner layer, *Nat. Commun.*, 2020, **11**, 3315.

37 M. Wang, R. Song, X. Zhang, G. Liu, S. Xu, Z. Xu, J. Liu and G. Qiao, Defects engineering promotes the electrochemical hydrogen evolution reaction property of phosphorene surface, *Int. J. Hydrogen Energy*, 2021, **46**, 1913–1922.

38 X. Shi, X. Zheng, H. Wang, H. Zhang, M. Qin, B. Lin, M. Qi, S. Mao, H. Ning and R. Yang, *et al.*, Hierarchical Crystalline/Amorphous Heterostructure MoNi/NiMoOx for Electrochemical Hydrogen Evolution with Industry-Level Activity and Stability, *Adv. Funct. Mater.*, 2023, 2307109.

39 X. Zhang, Z. Zhou, D. Zhang, J. Chen, J. Zhang and Z. Wang, Mixed-phase $MoTe_2$ with exposed edges and rich defects for catalyzing hydrogen evolution reaction with noble-metal-like performance, *Electrochim. Acta*, 2023, **457**, 142455.

40 D. P. Jaihindh, P. Anand, R.-S. Chen, W.-Y. Yu, M.-S. Wong and Y.-P. Fu, Cl-doped CuO for electrochemical hydrogen evolution reaction and tetracycline photocatalytic degradation, *J. Environ. Chem. Eng.*, 2023, **11**, 109852.

41 W. Wang, Y. Li, M. Li, H. Shen, W. Zhang, J. Zhang, T. Liu, X. Kong and H. Bi, Metallic phase WSe_2 nanoscrolls for the hydrogen evolution reaction, *New J. Chem.*, 2022, **46**, 8381–8384.

42 X. Zhao, K. Liu, F. Guo, Z. He, L. Zhang, S. Lei, H. Li, Y. Cheng and L. Yang, Meta-Position synergistic effect induced by Ni–Mo Co-doped WSe_2 to enhance the hydrogen evolution reaction, *Dalton Trans.*, 2022, **51**, 11758–11767.

43 G. Kresse and J. Hafner, Ab initio molecular dynamics for liquid metals, *Phys. Rev. B: Condens. Matter Mater. Phys.*, 1993, **47**, 558.

44 G. Kresse, J. Furthmüller and J. Hafner, Theory of the crystal structures of selenium and tellurium: the effect of generalized-gradient corrections to the local-density approximation, *Phys. Rev. B: Condens. Matter Mater. Phys.*, 1994, **50**, 13181.

45 G. Kresse and J. Furthmüller, Efficient iterative schemes for ab initio total-energy calculations using a plane-wave basis set, *Phys. Rev. B: Condens. Matter Mater. Phys.*, 1996, **54**, 11169.

46 J. P. Perdew, K. Burke and M. Ernzerhof, Generalized gradient approximation made simple, *Phys. Rev. Lett.*, 1996, **77**, 3865.

47 H. Liu, R. Xie, Y. Luo, Z. Cui, Q. Yu, Z. Gao, Z. Zhang, F. Yang, X. Kang and S. Ge, *et al.*, Dual interfacial engineering of a Chevrel phase electrode material for stable hydrogen evolution at 2500 mA cm^{-2}, *Nat. Commun.*, 2022, **13**, 6382.

48 Y. Tong, D. Feng and P. Chen, Dual modification strategy of nickel sulfide as pH-universal catalysts for hydrogen production at large current density, *ACS Sustainable Chem. Eng.*, 2021, **9**, 10601–10610.

49 Y. Chen, G. Yu, W. Chen, Y. Liu, G.-D. Li, P. Zhu, Q. Tao, Q. Li, J. Liu and X. Shen, *et al.*, Highly active, nonprecious electrocatalyst comprising borophene subunits for the hydrogen evolution reaction, *J. Am. Chem. Soc.*, 2017, **139**, 12370–12373.

50 H. Zhou, F. Yu, J. Sun, H. Zhu, I. K. Mishra, S. Chen and Z. Ren, Highly efficient hydrogen evolution from edgeoriented $WS_{2(1-x)}Se_{2x}$ particles on three-dimensional porous $NiSe_2$ foam, *Nano Lett.*, 2016, **16**, 7604–7609.

51 C. Zhang, Y. Luo, J. Tan, Q. Yu, F. Yang, Z. Zhang, L. Yang, H.-M. Cheng and B. Liu, High-throughput production of cheap mineral-based two-dimensional electrocatalysts for high-current–density hydrogen evolution, *Nat. Commun.*, 2020, **11**, 3724.

52 D. Zhang, F. Wang, W. Zhao, M. Cui, X. Fan, R. Liang, Q. Ou and S. Zhang, Boosting hydrogen evolution reaction activity

of amorphous molybdenum sulfide under high currents via preferential electron filling induced by tungsten doping, Advanced, *Science*, 2022, **9**, 2202445.

53 I. K. Mishra, H. Zhou, J. Sun, F. Qin, K. Dahal, J. Bao, S. Chen and Z. Ren, Hierarchical CoP/Ni_5P_4/CoP microsheet arrays as a robust pH-universal electrocatalyst for efficient hydrogen generation, *Energy Environ. Sci.*, 2018, **11**, 2246–2252.

54 J. Sun, M. Ren, L. Yu, Z. Yang, L. Xie, F. Tian, Y. Yu, Z. Ren, S. Chen and H. Zhou, Highly efficient hydrogen evolution from a mesoporous hybrid of nickel phosphide nanoparticles anchored on cobalt phosphosulfide/phosphide nanosheet arrays, *Small*, 2019, **15**, 1804272.

55 M. Das, N. Jena, T. Purkait, N. Kamboj, A. De Sarkar and R. S. Dey, Single-phase Ni_5P_4–copper foam superhydrophilic and aerophobic core–shell nanostructures for efficient hydrogen evolution reaction, *J. Mater. Chem. A*, 2019, **7**, 23989–23999.

56 Y. Luo, L. Tang, U. Khan, Q. Yu, H.-M. Cheng, X. Zou and B. Liu, Morphology and surface chemistry engineering toward pH-universal catalysts for hydrogen evolution at high current density, *Nat. Commun.*, 2019, **10**, 269.

57 L. Zhang, Z. Yan, X. Chen, M. Yu, F. Liu, F. Cheng and J. Chen, Facile synthesis of amorphous MoS_x–Fe anchored on Zr-MOFs towards efficient and stable electrocatalytic hydrogen evolution, *Chem. Commun.*, 2020, **56**, 2763–2766.

58 L. Zhu, H. Lin, Y. Li, F. Liao, Y. Lifshitz, M. Sheng, S.-T. Lee and M. Shao, A rhodium/silicon co-electrocatalyst design concept to surpass platinum hydrogen evolution activity at high overpotentials, *Nat. Commun.*, 2016, **7**, 12272.

59 J. Yang, A. R. Mohmad, Y. Wang, R. Fullon, X. Song, F. Zhao, I. Bozkurt, M. Augustin, E. J. Santos and H. S. Shin, *et al.*, Ultrahigh-current–density niobium disulfide catalysts for hydrogen evolution, *Nat. Mater.*, 2019, **18**, 1309–1314.

60 G. Li, J. Yu, J. Jia, L. Yang, L. Zhao, W. Zhou and H. Liu, Cobalt–Cobalt Phosphide Nanoparticles@Nitrogen-Phosphorus Doped Carbon/Graphene Derived from Cobalt Ions Adsorbed Saccharomycete Yeasts as an Efficient, Stable, and Large-Current–Density Electrode for Hydrogen Evolution Reactions, *Adv. Funct. Mater.*, 2018, **28**, 1801332.

61 Z. Zhang, Y. Wang, X. Leng, V. H. Crespi, F. Kang and R. Lv, Controllable edge exposure of MoS_2 for efficient hydrogen evolution with high current density, *ACS Appl. Energy Mater.*, 2018, **1**, 1268–1275.

62 S. Riyajuddin, K. Azmi, M. Pahuja, S. Kumar, T. Maruyama, C. Bera and K. Ghosh, Super-hydrophilic hierarchical Ni-foam-graphene-carbon nanotubes-Ni_2P–CuP_2 nanoarchitecture as efficient electrocatalyst for overall water splitting, *ACS Nano*, 2021, **15**, 5586–5599.

63 Z. Zhongming, L. Linong, Y. Xiaona, Z. Wangqiang and L. Wei, *et al.*, Design of Aligned Porous Carbon Films with Single-Atom Co-NC Sites for High-Current–Density Hydrogen Generation, *Adv. Mater.*, 2021, **33**, 2103533.

64 C. Huang, L. Yu, W. Zhang, Q. Xiao, J. Zhou, Y. Zhang, P. An, J. Zhang and Y. Yu, N-doped Ni–Mo based sulfides for highefficiency and stable hydrogen evolution reaction, *Appl. Catal., B*, 2020, **276**, 119137.

65 C. Jian, Q. Cai, W. Hong, J. Li and W. Liu, Edge-riched $MoSe_2$/MoO_2 hybrid electrocatalyst for efficient hydrogen evolution reaction, *Small*, 2018, **14**, 1703798.

66 X. Cao, L. Zhang, K. Huang, B. Zhang, J. Wu and Y. Huang, Strained carbon steel as a highly efficient catalyst for seawater electrolysis, *Energy Mater.*, 2022, **2**, 200010.

67 C. C. McCrory, S. Jung, J. C. Peters and T. F. Jaramillo, Benchmarking heterogeneous electrocatalysts for the oxygen evolution reaction, *J. Am. Chem. Soc.*, 2013, **135**, 16977–16987.

68 L. Li, C. Liu, S. Liu, J. Wang, J. Han, T.-S. Chan, Y. Li, Z. Hu, Q. Shao and Q. Zhang, *et al.*, Phase engineering of a ruthenium nanostructure toward high-performance bifunctional hydrogen catalysis, *ACS Nano*, 2022, **16**, 14885–14894.

69 J. Gu, L. Li, Y. Xie, B. Chen, F. Tian, Y. Wang, J. Zhong, J. Shen and J. Lu, Turing structuring with multiple nanotwins to engineer efficient and stable catalysts for hydrogen evolution reaction, *Nat. Commun.*, 2023, **14**, 5389.

70 D. Vikraman, S. Hussain, I. Rabani, A. Feroze, M. Ali, Y.-S. Seo, S.-H. Chun, J. Jung and H.-S. Kim, Engineering $MoTe_2$ and Janus SeMoTe nanosheet structures: firstprinciples roadmap and practical uses in hydrogen evolution reactions and symmetric supercapacitors, *Nano Energy*, 2021, **87**, 106161.

71 B. Hinnemann, P. G. Moses, J. Bonde, K. P. Jørgensen, J. H. Nielsen, S. Horch, I. Chorkendorff and J. K. Nørskov, Biomimetic hydrogen evolution: MoS_2 nanoparticles as catalyst for hydrogen evolution, *J. Am. Chem. Soc.*, 2005, **127**, 5308–5309.